HiSAC: High-Resolution Sensing with Multiband Communication Signals

Jacopo Pegoraro
jacopo.pegoraro@unipd.it
University of Padova
Padova, Italy

Jesus O. Lacruz
jesusomar.lacruz@imdea.org
IMDEA Networks Institute
Madrid, Spain

Michele Rossi
michele.rossi@unipd.it
University of Padova
Padova, Italy

Joerg Widmer
joerg.widmer@imdea.org
IMDEA Networks Institute
Madrid, Spain

ABSTRACT

Integrated Sensing And Communication (ISAC) systems are expected to perform accurate radar sensing while having minimal impact on communication. Ideally, sensing should only *reuse* communication resources, especially for spectrum which is contended by many applications. However, this poses a great challenge in that communication systems often operate on narrow subbands with low sensing resolution. Combining contiguous subbands has shown significant resolution gain in active localization. However, multiband ISAC remains unexplored due to communication subbands being highly sparse (*non-contiguous*) and affected by phase offsets that prevent their aggregation (*incoherent*). To tackle these problems, we design HiSAC, the first multiband ISAC system that combines diverse subbands across a wide frequency range to achieve super-resolved passive ranging. To solve the non-contiguity and incoherence of subbands, HiSAC combines them progressively, exploiting an anchor propagation path between transmitter and receiver in an optimization problem to achieve phase coherence. HiSAC fully reuses pilot signals in communication systems, applies to different frequencies, and can combine diverse technologies, e.g., 5G-NR and WiGig. We implement HiSAC on an experimental platform in the millimeter-wave unlicensed band and test it on objects and humans. Our results show it enhances the sensing resolution by up to 20 times compared to single-band processing while occupying the same spectrum.

CCS CONCEPTS

• **Hardware → Signal processing systems**; • **Human-centered computing → Ubiquitous and mobile computing**; • **Applied computing → Telecommunications**.

KEYWORDS

Integrated sensing and communications, human sensing, multiband, super-resolution, Wi-Fi sensing, 5G.

SENSYS '24, November 4–7, 2024, Hangzhou, China

ACM ISBN 979-8-4007-0697-4/24/11.
https://doi.org/10.1145/3666025.3699357

ACM Reference Format:
Jacopo Pegoraro, Jesus O. Lacruz, Michele Rossi, and Joerg Widmer. 2024. HiSAC: High-Resolution Sensing with Multiband Communication Signals. In *The 22nd ACM Conference on Embedded Networked Sensor Systems (SENSYS '24), November 4–7, 2024, Hangzhou, China.* ACM, New York, NY, USA, 15 pages. https://doi.org/10.1145/3666025.3699357

1 INTRODUCTION

Endowing wireless communication systems with radar sensing capabilities is one of the key objectives of 3GPP Sixth Generation (6G) and future Wi-Fi [30]. In recent years, so-called Integrated Sensing And Communication (ISAC) systems have enabled a wide range of applications from multitarget tracking [37, 53], person identification [38, 58], activity recognition [26, 32], vital signs monitoring [60], pose estimation [12, 14], and object imaging [59, 65].

Motivation. A fundamental trade-off in ISAC systems is to achieve high sensing resolution, i.e., the capability of distinguishing multiple closely located targets, and accuracy with minimal impact on the primary communication functionality. Ideally, sensing should be performed by fully reusing resources available to the communication system in time and frequency. Particular attention has to be put on spectrum, which is becoming increasingly scarce due to the ubiquitous applications of Radio Frequency (RF) transmissions [45]. Indeed, ISAC benefits from using a large bandwidth since this is inversely proportional to the ranging resolution, i.e., the minimum signal propagation distance below which two targets can not be distinguished. Note that enhancing ranging resolution is also highly beneficial to advanced sensing applications such as human respiration monitoring. Although small chest displacements can be monitored even with a narrowband signal [64], using the carrier phase, separating the respiration of multiple closely-located subjects with low ranging resolution is extremely challenging and prone to errors

However, the bandwidth available to existing communication systems is insufficient to achieve the desired *cm-level ranging* resolution in 6G. Even wideband Fifth Generation-New Radio (5G-NR) channels and IEEE 802.11ay (WiGig) in the Millimeter Wave (mmWave) band can at most reach 37 cm and 17 cm resolution with 400 MHz and 1.76 GHz bandwidth, respectively. Such resolution can be improved by applying super-resolution algorithms based on MUltiple SIgnal Classification (MUSIC) or compressed sensing, e.g., [16, 18, 42], but the bandwidth limitation remains.

A possible solution to enhance the resolution is to *combine* multiple communication frequency bands to increase the sensing bandwidth. This approach has been attempted for active localization in Orthogonal Frequency Division Multiplexing (OFDM) systems (where the user carries a communication device) [18, 35, 52, 57], radar [8, 56, 69], and recently for sub-6 GHz Wi-Fi sensing in [24]. However, several limitations make the above methods unsuitable for ISAC. On the one hand, active localization approaches exploit either contiguous or closely-spaced subbands, which may not be available in ISAC since the spectrum is contended by a plethora of services and contains frequency gaps. Moreover, they can count on a *collaborative* localized device, which simplifies the problem since synchronization errors that prevent accurate delay measurements can be resolved via handshaking [16]. On the other hand, radar methods use dedicated waveforms, optimized for sensing purposes, and relatively wide subbands to be combined, which significantly simplifies the problem. Lastly, [24] employs a neural network model to overcome the above limitations in Wi-Fi, but this ties the system to the specific frequency band, communication technology (Wi-Fi), and hardware used to collect the training data. Conversely, we aim to develop a system that seamlessly adapts to different modulation types such as 5G-NR OFDM and IEEE 802.11ay Single Carrier (SC).

Challenges. Designing such a system presents several open challenges. First, one must tackle the non-contiguity of communication systems subbands, which may include gaps of several hundreds of MHz or even GHz. Second, the different subbands are affected by time-varying and unknown timing, frequency, and phase offsets that prevent the coherent combination of the Channel Frequency Response (CFR) estimated by the communication protocol over different ISAC receivers (RXs) [54, 68]. Although the compensation of timing and frequency offsets in ISAC systems has been widely studied [25, 34, 36, 62, 70], *phase* synchronization is not well investigated since it is not needed in typical sensing tasks such as target tracking and Doppler estimation. On the contrary, achieving phase coherence is a strict requirement to combine multiple subbands over a wide frequency range. Third, communication subbands are relatively narrow with respect to the total bandwidth required to achieve high resolution. This makes it difficult to model individual subbands as they contain insufficient frequency samples. Conversely, reconstructing the CFR over the total bandwidth entails huge computational complexity due to the high number of subcarriers. Finally, the designed method should generalize to different communication systems (OFDM vs. SC), protocols (5G-NR vs. Wi-Fi), and channel representations (e.g., CFR vs. Channel Impulse Response (CIR)).

Contribution. To address these challenges, we design and validate HiSAC, the first multiband ISAC system that fully reuses communication traffic across multiple bands (and technologies) to boost the sensing resolution, as shown in Fig. 1. HiSAC first combines all the subbands used by the same ISAC transmitter (TX)-RX pair (a *subsystem*), which are affected by the same offsets and hence phase-coherent. Then, it compensates for relative timing, frequency, and phase offsets across different subsystems, which are instead incoherent. For this, a new *phase synchronization* algorithm is proposed based on a simple, yet effective, initialization, based on an anchor propagation path, and refinement through an optimization problem. Then, HiSAC combines all the available subbands across

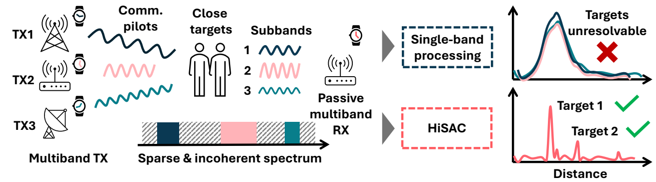

Figure 1: Overview of HiSAC's multiband sensing.

subsystems with a focused Orthogonal Matching Pursuit (OMP) algorithm [10] that exploits the (coarse) prior knowledge about targets' locations obtained from the single subsystems, and outputs super-resolved range estimates. As a final step, HiSAC can combine range estimates obtained from different packets or OFDM slots *over time* (coherently or incoherently) to further boost the resolution and accuracy. Our approach combines subbands over several GHz of bandwidth, fully reusing pilot signal in communication systems, e.g., Synchronization Signal Blocks (SSBs) in 5G-NR, and applies to different frequencies, communication systems, and even different technologies, e.g., SC and OFDM.

We implement HiSAC on a Radio Frequency System on a Chip (RFSoC) platform in the mmWave unlicensed band (58-64 GHz). We demonstrate that HiSAC achieves a few-cm ranging resolution on metal and human targets, giving a 3 to 20 times improvement over baseline methods. Moreover, it works in mono-/bi-static configurations on typical multiband systems employing carrier aggregation, bandwidth part, and it is robust to target motion.

The contributions of our work can be summarized as:

1. We propose HiSAC, the first *multiband* ISAC system that achieves super-resolution passive ranging using non-contiguous, narrow, and incoherent subbands estimated by sets of communication pilot signals over time.
2. HiSAC features new model-based signal processing steps to achieve phase-coherence among subbands that adapt to different systems and technologies across GHz-wide bands.
3. Our approach entails zero additional overhead on communication and seamlessly integrates with multiband communication systems that adopt carrier aggregation or bandwidth part.
4. We prototype HiSAC in the unlicensed mmWave band and test it on a vast experimental campaign, showing it can achieve up to 20 times better resolution compared to a single band with the same spectrum occupation per time slot.

2 PRELIMINARIES AND MOTIVATION

In this section, we provide useful background on the applicability of HiSAC in ISAC systems, ranging resolution, and phase incoherence due to phase offsets. Then, we highlight the novelty of our approach with respect to existing active multiband systems for localization.

2.1 HiSAC use cases in ISAC

Multiband operation is widely used in communications to increase the data rate and multiplex applications to different users. In this section, we provide an overview of three practical use cases of our method for multiband ISAC: Two of them are typical of cellular networks, such as 5G-NR or future 6G, and one tackles cross-technology multiband sensing.

Carrier aggregation. Carrier aggregation is a function implemented in the Radio Access Network (RAN) and User Equipments (UEs) of 5G-NR mobile wireless networks. carrier aggregation combines multiple frequency allocations (carriers) at different radio cells to boost the data rate of the connection [23]. A set of serving cells is identified that contributes to the aggregation, which can take place within the same frequency band (intra-band), e.g., within the sub-6 GHz range, or across multiple bands (inter-band), e.g., across Frequency Range (FR) 2 and FR 3. Exploiting the channel estimation process carried out on each frequency band for sensing would greatly enhance the available bandwidth and, as a result, the ranging resolution.

Bandwidth part. Bandwidth part is a mechanism to split the radio channel available to a cell into multiple segments (*parts*), which can then be used to allocate different regions of the spectrum to different applications (or UEs) [27]. Only one part can be active at a time, and SSBs can be transmitted in each part to synchronize to different UEs. Given that SSBs have a relatively narrow bandwidth, it is appealing to develop a system that can combine the SSBs transmitted by one or more radio cells to perform accurate mono-static ranging by exploiting the total frequency aperture over a wider bandwidth. Note that, bandwidth part poses the additional requirement that the system must be able to operate with CFR estimates that are not collected simultaneously in all the subbands.

Cross-technology multiband processing. Coexistence of *unlicensed* 5G-NR and IEEE 802.11ay has been advocated in the 60 GHz band and has gathered significant interest from academia and industry [9, 39]. Flexible multiband processing across OFDM and SC communication technologies is appealing to boost sensing resolution in these cases. While combining multiple Wi-Fi channels has been studied for both communication [4] and localization [18, 57], combining multiple frequency bands obtained by Wi-Fi and cellular communication systems is still unexplored. In the mmWave band, IEEE 802.11ay channels span a wide bandwidth of 1.76 GHz, while in 5G-NR channels are limited to 400 MHz. Therefore, combining multiple channels across the two technologies can yield practical Ultra-Wide Band (UWB)-level resolution with CFR estimates spanning several GHz of bandwidth.

2.2 Delay and ranging resolution

The delay resolution, $\Delta\tau$, of a localization or passive sensing system is related to the bandwidth, B, of the transmission signal as $\Delta\tau = 1/B$. The corresponding ranging resolution for passive sensing also depends on the angle between the segments connecting the TX to the target and the target to the RX (*bi-static* angle), β, as $\Delta r = c/[2B\cos(\beta/2)]$. A mono-static system, with co-located TX and RX, gives $\Delta r = c/(2B)$ which minimizes Δr with respect to β. Unlike radar systems, which typically feature a large transmission bandwidth fully dedicated to sensing, communication systems are relatively narrowband for sensing purposes. As an example, even mmWave 5G-NR system with 400 MHz channels can only reach up to 37 cm mono-static ranging resolution, which may be insufficient for fine-grained sensing applications. Moreover, such resolution is only obtained if the full bandwidth is used to estimate the channel. This is often not the case, since pilot signals are transmitted on a subset of the available subcarriers. The SSBs used for synchronization with UEs, for example, occupy 240 OFDM subcarriers with at most 240 kHz subcarrier spacing. This leads to a very coarse ranging resolution of $\Delta r = c/(2 \cdot 240 \cdot 240\text{kHz}) = 2.6$ m.

Improving ranging resolution is a challenging task since the bi-static angle depends on the location of the TX, RX, and target, and increasing the bandwidth is not viable in ISAC systems since it is pre-determined by the communication protocol. Super-resolution approaches have been proposed that exploit subspace-based methods, e.g., MUSIC [18], or compressed sensing algorithms [17], exploiting assumptions on the structure of the channel (e.g., sparsity). However, none of these methods can drastically improve the ranging resolution, and limitations due to the narrow bandwidth remain.

2.3 Phase-incoherence among subbands

In a wireless communication system, the clock signal of each node is generated from a Local Oscillator (LO). The different LOs are asynchronous, meaning that, due to hardware non-idealities, they are subject to time-varying relative drifts from their nominal oscillating frequencies [67]. In addition, their initial phase is random. This introduces unwanted offsets in the received signals that are specific to each TX-RX pair. These can be categorized into Timing Offset (TO), Carrier Frequency Offset (CFO), and Random Phase Offset (RPO) [54].

TO results from the lack of time synchronization between the TX and RX. It is due to the unknown shift or offset affecting the RX clock relative to the TX one, and to the synchronization point chosen by the RX. TO is time-varying and causes an undesired phase term that increases linearly with the subcarriers in OFDM systems.

CFO is due to the time-varying difference in the LOs of the TX and RX. Communication systems typically estimate and partially compensate for the CFO. This leads to a residual CFO that is fast time-varying, as a result of the compensation error [54]. CFO causes a cumulative phase shift across packets or OFDM slots.

The RPO can be caused by non-idealities in the TX and RX devices, as well as by phase noise [40]. It varies on an OFDM symbol basis. Note that RPO can be present even between the multiple channels of the same LO.

When multiple ISAC systems in different frequency bands are considered, a direct combination of their CFRs is infeasible due to the presence of the above offsets. Indeed, this causes the phases of the CFRs in the different bands to be misaligned at the different RXs, preventing the construction of a common model spanning the full frequency band. Several approaches have been proposed to tackle TO and CFO in ISAC systems [5, 25, 32, 34, 36, 60–62, 70]. However, none of these tackles phase synchronization by also eliminating the RPO, which is essential for multiband CFR combination.

2.4 Innovation over multiband localization

Exploiting multiple frequency bands for localizing an *active* receiver device has been widely studied. HiSAC instead tackles the different problem of *passive* ranging, in which the target of the localization is an object or person, not necessarily equipped with a radio device.

Two main aspects prevent the application of existing methods for active localization to the passive ISAC scenario.

First, active localization targets the time-of-arrival estimation of the Line-of-Sight (LOS) path between TX and RX, as done by Chronos [49] and SpotFi [18], among others [3, 16]. Hence, multipath reflections are regarded as a nuisance and have to be compensated for. Conversely, our work focuses on obtaining the propagation delays of reflections on passive objects that are causing the multipath effect. These are significantly weaker than the LOS, due to the longer propagation distance and scattering on the target. The applicability of active localization methods for paths other than the LOS has not been demonstrated, making them unsuitable for radar-like sensing, which is the objective of HiSAC.

Second, existing multiband localization methods combine overlapping, contiguous, or relatively close frequency subbands [18, 55, 57]. This is due to the limitations of existing algorithms to achieve phase coherence, which do not scale well to wide frequency bands, and the high computational complexity of compressed sensing. Due to these limitations, existing methods can not be applied to ISAC, where subbands may be widely separated in frequency as discussed in Section 2.1, with a low ratio of measured frequencies over the total bandwidth aperture. We demonstrate instead that HiSAC can accurately perform ranging with as low as 1/6 measured frequencies ratio (see Section 6.2). This is enabled by exploiting the channel sparsity, originally applying compressed sensing in two incremental steps to reduce complexity, and to the increased robustness of HiSAC's phase offsets compensation method. Thanks to these innovations, HiSAC is also the first multiband system that demonstrates *cross-technology* sensing capabilities, combining OFDM and SC channel estimates over wide bands.

Third, active localization relies on *information exchange* among nodes to compensate for phase offsets, which introduces overhead on communication and energy consumption. Multiband methods like Chronos [49], Owll [3], M^3 [6], and others [16, 17] exchange channel measurements using dedicated handshaking protocols and perform active frequency hopping. The overhead due to these additional transmissions reduces the Wi-Fi throughput by 18.5% in Chronos [49], while [3] shows their significant impact on the battery life of embedded devices. Conversely, HiSAC does not require exchanging channel estimates or performing frequency hopping. It only uses channel estimates that are *already available* at the receiver, without introducing any further cooperation or information exchange (i.e., avoiding the involved communication overhead).

3 SYSTEM MODEL

In this section, we formulate a general model of a multiband ISAC system that fits all the use cases in Section 2.1.

3.1 Non-coherent subsystems and subbands

Consider a wide frequency band with bandwidth B and starting frequency f_0, denoted as the *full band* of interest, as shown in Fig. 2. The full band represents the total frequency aperture of HiSAC, which gives the ideal delay resolution of the system. In practice, the full band may represent the total aperture of carrier aggregation or bandwidth part systems, spanning from the frequency of the first estimated subcarrier in the channel response to the last one, including frequency gaps.

We call Δ_f the spacing of the frequency samples of the considered CFR (subcarriers). Δ_f corresponds to the subcarrier spacing in OFDM systems or to the Discrete Fourier Transform (DFT) samples spacing used in SC systems. The total number of *virtual* subcarriers in the full band is $K = B/\Delta_f$, indexed by $k = 0, \dots, K-1$. We use the term virtual to highlight that not all the subcarriers are used for communication, which is carried out on a subset of the full band spectrum. In the following, we assume that all the considered subbands share the same subcarrier spacing Δ_f, which can be achieved using interpolation or downsampling.

We consider an ISAC system consisting of C non-coherent subsystems affected by TO, CFO, and RPO. Each subsystem, i, includes one TX-RX pair that may be co-located (*mono-static*) or widely separated (*bi-static*). In practice, a subsystem can be represented by co-located Base Stations (BSs) or Access Points (APs) from different operators, acting as mono-static ISAC transceivers, or BS-BS/BS-UE pairs in the bi-static case. Subsystem i has bandwidth B_i, starting from frequency f_i, contained in the full band. The total number of virtual subcarriers of a subsystem is $K_i = B_i/\Delta_f$. Within each subsystem, the channel is estimated over a set $\mathcal{S}_i$ of potentially non-contiguous subbands, with $|\mathcal{S}_i| = S_i$. The subbands may span the whole B_i or a part of it, according to the allocation of pilot signals used for channel estimation. We use index $s = 1, \dots, S_i$ to identify the subbands in subsystem i. Note that S_i may equal 1 if system i has a single subband. We call the total number of subbands in the system $S = \sum_{i=1}^{C} S_i$. Each subband contains a set of $K_{i,s}$ subcarriers. The subcarriers in the system for which the channel is estimated are called *available* subcarriers. The number of available subcarriers is $M_i = \sum_{s=1}^{S_i} K_{i,s}$, for subsystem i and $M = \sum_{i=1}^{C} M_i$ for the whole system, with $M_i \leq K_i$ and $M < K$.

Note that HiSAC handles subsystems and subbands with different bandwidths, which is critical to seamlessly integrate it into communication systems operating in diverse frequency bands.

Since each ISAC subsystem has a single RX, all the subbands of the same subsystem i share the same TO, CFO, and RPO due to being implemented on the same radio device. In our model, we consider TO, CFO, and RPO of subsystem i to be relative to the first subsystem ($i = 1$), which we take as a reference. Hence, we denote by $\tau_{o,i}(t)$, $f_{o,i}(t)$, and $\varphi_{o,i}(t)$ the relative TO, CFO, and RPO of subsystem i, respectively. The absolute offsets do not impact the performance of our system and are omitted in the model.

3.2 Multiband channel model

In this section, we present the multiband CFR model. We consider a time-varying multipath channel with L propagation paths, where t is used to denote time. We denote by $\tau_l(t)$ and $\alpha_l(t)$ the delay of the l-th channel path due to propagation and its complex amplitude at time t, accounting for the combined effect of the propagation loss and the target's scattering phase [41]. Tab. 1 summarizes the notation used in the system model.

We model the CFR over the full band, discretized by the subcarrier spacing Δ_f. The expression of the full band CFR for subcarrier k at time t is

$$H_k(t) = \sum_{l=1}^{L} \alpha_l(t) e^{-j2\pi k \Delta_f \tau_l(t)}, \quad k = 0, \dots, K-1, \qquad (1)$$

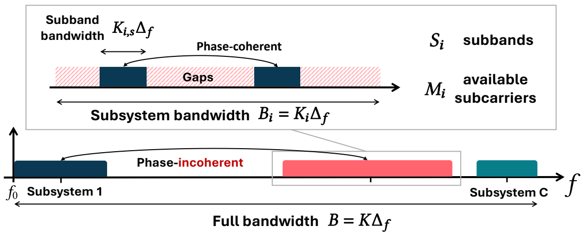

Figure 2: Summary of subsystems and subbands notation.

Start frequency	f_0	No. avail. subc. subsys. i	M_i
Full bandwidth	B	TO subsystem i	$\tau_{o,i}$
Subcarrier spacing	Δ_f	CFO subsystem i	$f_{o,i}$
Total no. subcarriers	K	RPO subsystem i	$\varphi_{o,i}$
No. of subsystems	C	PO subsystem i	$\phi_{o,i}$
No. subcarriers subsys. i	K_i	Total delay resolution	$\Delta\tau$
No. subc. subsys. i subb. s	$K_{i,s}$	Number of paths	L
Start frequency subsys. i	f_i	Complex gain path l	α_l
Bandwidth subsystem i	B_i	Delay path l	τ_l
Subbands set subsystem i	$\mathcal{S}_i$	Start idx. subsys. i subb. s	$k_{i,s}$
No. subbands subsystem i	S_i	k-th subc. in total CFR	H_k
No. available subcarriers	M	k-th subc. subsys. i subb. s	$H_{i,s,k}$

Table 1: Summary of the notation.

with delay resolution $\Delta\tau = 1/(\Delta_f K)$. The CIR can be obtained from the CFR via an Inverse DFT (IDFT) along the subcarriers. Note that, in Eq. (1), we include the carrier phase into each path's complex amplitude $\alpha_l(t)$. Considering the carrier phase in the full band channel model would lead to high sensitivity of the algorithm to errors in the positioning of the TX and RX antennas of each subsystem, which would make it impractical to use. This is especially true for at mmWave frequencies where the wavelength is short. Hence, HiSAC exploits the bandwidth aperture B, rather than the carrier f_0. As commonly done in the UWB channels literature [50, 51], we consider the coefficients $\alpha_l(t)$ to be constant within the frequency band of interest. This holds if the total bandwidth is less than 20% of the carrier frequency [33].

We denote by $k_{i,s}$ the starting index of subband s in subsystem i in the full band grid, $k = 0, \dots, K$. The CFR in subband s, at subcarrier $\kappa = 0, \dots, K_{i,s} - 1$, is

$$H_{i,s,\kappa}(t) = e^{j\phi_{o,i}(t)} e^{-j2\pi\kappa\Delta_f\tau_{o,i}(t)} \sum_{l=1}^{L} \alpha_l(t) e^{-j2\pi(k_{i,s}+\kappa)\Delta_f\tau_l(t)}, \tag{2}$$

where $\phi_{o,i}(t) = -2\pi f_{o,i}(t)t + \varphi_{o,i}(t)$ is denoted by Phase Offset (PO) in the following. The PO contains the contribution of the CFO and the RPO since these are constant in κ and l.

4 HISAC METHODOLOGY

This section presents HiSAC's processing steps, which are summarized in the following and shown in Fig. 3.

(1) Coherent intra-subsystem combination. The first step performs a coarse multiband reconstruction of the CFR, using only the coherent subbands in each subsystem, as detailed in Section 4.1. The reason to first aggregate subbands over each subsystem is to obtain a wider-band CFR, to simplify the subsequent removal of phase offsets.

(2) TO and PO compensation. This step applies a new algorithm to achieve phase synchronization across multiple subsystems, making them suitable for coherent multiband combination (see Section 4.2). Compared to existing approaches, ours is more robust with narrow, non-contiguous subbands by (i) exploiting an anchor path for TO initialization and (ii) accurately estimating TO and PO via optimization.

(3) Inter-subsystem multiband reconstruction. Delays and amplitudes of the multipath components in the CFR are estimated using all the available subbands. This is done with the OMP algorithm, to tackle the gaps in the CFR measurements, by restricting the search space around the initial estimates obtained from the coherent subsystems to counter the discretization error, as detailed in Section 4.3.

(4) Temporal aggregation. HiSAC can optionally aggregate the estimates of the multipath parameters across time, represented by different packets or OFDM slots. The aggregation consists of an accumulation and selection algorithm, that yields significantly improved ranging accuracy and resolution after a few time slots (see Section 4.4).

Steps (1)-(3) do not depend on the time instant in which the CFR is estimated, so we omit the time t in their description.

4.1 Intra-subsystem coherent combination

As a first step, we combine the subbands obtained by each subsystem i coherently (since they experience the same TO and PO) to coarsely estimate the multipath delays and complex amplitudes. To do so, we first observe that the CFR in Eq. (1) is *sparse* in the delay domain. This stems from the fact that in typical communication channels the number of paths, L, is much lower than the number of total subcarriers, K. Hence, it is possible to represent the CFR as a combination of much fewer basis signals compared to the number of subcarriers. This fact can be exploited to recover the CFR for subsystem i from the incomplete set of M_i CFR measurements, according to the compressed sensing principle [10].

Notation and definitions. To formulate the intra-subsystem CFR reconstruction as a compressed sensing problem, we set up a grid with Q_i channel path candidates as $0, \dots, (Q_i - 1)\delta_i$, where δ_i is the grid granularity of subsystem i. The size of the grid should be selected according to a trade-off between reconstruction performance and computational complexity. Each candidate is a complex sinusoidal signal that represents a possible channel path with its corresponding delay. To compactly represent the set of candidate paths, we construct a partial Fourier matrix, $\mathbf{F}_i$, that spans all the subcarriers in subsystem i and the delays in the grid. Element m, q of $\mathbf{F}_i$ is $(\mathbf{F}_i)_{m,q} = e^{j2\pi mq\delta_i\Delta_f}/\sqrt{K_i}$. The columns of $\mathbf{F}_i$ represent the different complex sinusoids corresponding to the candidate paths. However, in our multiband ISAC system not all the subcarriers are observed by subsystem i. To model this aspect, we define $\mathbf{A}_i$ as the matrix whose rows are the vectors of all zeros but the k-th component, which equals 1, with $k \in \{k_{i,1}, \dots, K_{i,1} - 1, \dots, k_{i,S}, \dots, K_{i,S} - 1\}$. We use $\mathbf{A}_i$ to select the rows of $\mathbf{F}_i$ whose indices are in the set of available CFR samples in subsystem i.

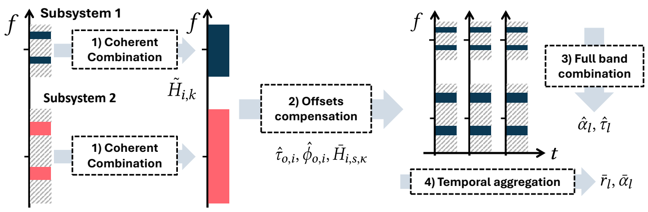

Figure 3: HiSAC high-level overview.

We obtain the final model matrix, which only contains the available parts of the complex sinusoids corresponding to the candidate paths, as $\mathbf{\Gamma}_i = \mathbf{A}_i\mathbf{F}_i$, of dimension $M_i \times K_i$. Then, we collect all the available CFR measurements in subsystem i into vector $\mathbf{H}_i = [H_{i,1,0}, \dots, H_{i,1,K_{i,1}-1}, \dots, H_{i,S,0}, \dots, H_{i,S,K_{i,S}-1}]^\mathsf{T}$, of dimension M_i.

Compressed sensing problem formulation. To represent the coarse CIR estimate obtained by fusing the S_i subbands in subsystem i, we use vector $\mathbf{h}_i$, of dimension K_i. $\mathbf{h}_i$ is related to the CFR in the i-th subsystem by the following model $\mathbf{H}_i = \mathbf{\Gamma}_i\mathbf{h}_i + \mathbf{w}_i$, where $\mathbf{w}_i$ is a complex Gaussian noise vector with element-wise variance equal to σ^2_w. Since the CFR is sparse in the delay domain, only a small fraction of the components of $\mathbf{h}_i$ are non-zero.

Estimating the non-zero components of $\mathbf{h}_i$ is the aim of the compressed sensing-based CFR reconstruction. Specifically, this can be done by solving the following optimization problem

$$\mathbf{h}_i = \arg\min_{\mathbf{h}} ||\mathbf{h}||_0 \text{ subject to } ||\mathbf{H}_i - \mathbf{\Gamma}_i\mathbf{h}||_2^2 < \epsilon, \tag{3}$$

where $||\cdot||_0$ is the number of non-zero components of a vector and ϵ is a pre-defined reconstruction error threshold that depends on the noise level.

OMP-based solution. To solve the problem in Eq. (3), we use the OMP algorithm [10], which operates by iteratively adding non-zero components to $\mathbf{h}_i$ in a greedy fashion. At each iteration, the candidate in $\mathbf{\Gamma}_i$ that best correlates with the residual measurements is selected as valid, and its complex amplitude is estimated via least-squares. The new valid candidate is then subtracted from the measurements and the process is repeated.

OMP finds an approximation to the sparsest estimate of the CIR that leads to a bounded Mean Squared Error (MSE) with the CFR measurements. The bound on the MSE is regulated by the positive constant ϵ, which can be estimated from the CFR estimates data. In our implementation, we stop the execution of OMP once the reconstruction error on the original measurements, $\mathbf{H}_i$, falls below 5% of the norm of $\mathbf{H}_i$.

We call L_i^{OMP} the number of non-zero components of $\mathbf{h}_i$ as reconstructed by OMP. Together with the complex coefficients of the valid candidate paths, OMP yields the corresponding path delays. We group the coefficients and delays into the set $\{\alpha_{i,l}, \tau_{i,l}\}$, $l = 1, \dots, L_i^{\text{OMP}}$. These correspond to the values and locations of the non-zero elements of vector $\mathbf{h}_i$ in the grid of candidates. Note that, since no phase offset compensation has been applied yet, $\tau_{i,l}$ is an estimate of $\tau_{1,l} + \tau_{o,i}$, i.e., the delays $\tau_{i,l}$ *contain the relative TO*. Finally, a synthetic CFR for subsystem i, is obtained as $\tilde{H}_{i,k} = \sum_{l=1}^{L_i^{\text{OMP}}} \alpha_{i,l} e^{-j2\pi k\Delta_f \tau_{i,l}}$, where k can be extended even outside of the subsystems' bandwidth. This will be used in the next section to compensate for relative TOs and POs.

4.2 Relative TO and PO compensation

In the second step, the relative TOs and POs among the different ISAC subsystems are compensated for. This is done by leveraging an *anchor* propagation path between the TX and the RX of each subsystem since the TO and PO are common to all paths [67]. The anchor path could be either the LOS path, which is commonly assumed to be available in ISAC [68], or a non-LOS static path seen by all subsystems. In the following, we first cast the TO and PO estimation as an optimization problem. Then, we detail how to exploit the anchor path in different subsystems to initialize the TO accurately. Finally, we solve the optimization and compensate for TO and PO to achieve phase-coherence.

Problem formulation. We compensate for $\tau_{o,i}$ and $\phi_{o,i}$ using the synthesized CFR of subsystem i and that of the reference subsystem. Intuitively, compensating for TO and PO amounts to performing the following two operations: (i) *phase-rotating* the complex values of the CFR of subsystem i, $\tilde{H}_{i,k}$, by $-\phi_{o,i}$ for all subcarriers, and (ii) *re-modulating* the CFR by multiplying it by the complex exponential $e^{j2\pi k\Delta_f \tau_{o,i}}$. It can be seen that applying (i) and (ii) cancels out the offsets from the CFR in Eq. (2).

As a result, TO and PO can be estimated by solving the following minimization problem

$$\begin{aligned}\{\hat{\tau}_{o,i}, \hat{\phi}_{o,i}\} &= \arg\min_{\tau,\phi} \sum_{k=0}^{K-1} \left|\tilde{H}_{1,k} - e^{-j\phi} e^{j2\pi k\Delta_f \tau} \tilde{H}_{i,k}\right|^2 \\ &= \arg\min_{\tau,\phi} \sum_{k=0}^{K-1} -2\mathrm{Re}\left\{e^{-j\phi} e^{j2\pi k\Delta_f \tau} \tilde{H}^*_{1,k} \tilde{H}_{i,k}\right\}, \end{aligned} \tag{4}$$

where * and $\mathrm{Re}\{\cdot\}$ are the complex conjugate and real part of a complex number, respectively. Solving Eq. (4) gives the phase rotation and re-modulation delay that best match the measured CFR on the reference subsystem. The problem is high-dimensional, non-linear, and non-convex, which causes solvers to converge to inaccurate solutions and get stuck in local minima. Moreover, its computational complexity is prohibitive since the number of frequency samples K is huge due to its relation with the subcarrier spacing.

Initialization. To solve the problem, we obtain an accurate initial estimate of the TO from the synthesized CFRs. We select the anchor path delay for subsystem i, denoted by $\tau_{i,1}$, among $\{\alpha_{i,l}, \tau_{i,l}\}$, $l = 1, \dots, L_i^{\text{OMP}}$. If this corresponds to the LOS, it is easily identifiable by having strong received power compared to scattered paths [20] and by having the smallest propagation delay. If the anchor path is a non-LOS static reflection, it can be localized by each subsystem before applying HiSAC. The path delays of the reference subsystem, $\tau_{1,1}$, are not affected by relative TO. Since the TO is common to *all* the propagation paths, it can be estimated from the anchor path and used to initialize the solution to Eq. (4). We estimate the relative TO as the difference between the anchor path delay of subsystem i and that of the reference subsystem, $\hat{\tau}'_{o,i} = \tau_{1,i} - \tau_{1,1}$. This reasoning is shown in Fig. 4a. The OMP grid step used in subsystem i, δ_i, limits the accuracy of $\hat{\tau}'_{o,i}$, since the values of $\tau_{1,i}$ can only lie on the grid. Therefore, we apply a refinement step to the TO estimate and also obtain the PO.

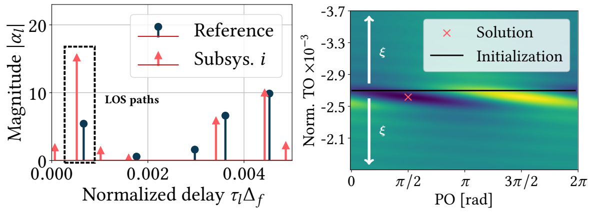

(a) Delay difference of the anchor paths initializes the TO.

(b) Cost function, yellow/blue represent high/low values.

Figure 4: Example estimation of the initialization value for the TO, (a), and the refinement via optimization, (b).

Initializing the TO estimate using delay differences is an innovation of HiSAC. It allows reducing the complexity of directly solving Eq. (4) by reducing the search space for the TO which, unlike the PO, is unbounded and causes fast oscillations of the cost function. Moreover, note that solving Eq. (4) requires achieving phase coherence between the recostructed CFRs across the *full* bandwidth. When the frequency bands of the subsystems are widely separated, this is challenging since even a small error on the TO can cause large phase variations across wide frequency bands. Existing methods based on linear fitting of the phase, e.g., [18], are prone to errors in these cases as we show in Section 6.

Refinement. Once the initial estimate of the TO has been obtained, we refine it by solving Eq. (4). The computational complexity is greatly reduced by searching over a small neighborhood of $\hat{\tau}'_{o,i}$, while for the PO we search over the interval $[0, 2\pi]$. We use a grid search for this optimization, focusing the search space in $[\hat{\tau}'_{o,i} - \xi, \hat{\tau}'_{o,i} + \xi]$ for the TO, where $\xi = 5\delta_i$, i.e., 5 times the OMP grid step of the subsystem. Note that this choice achieves a trade-off between reducing the search space as much as possible and accounting for errors in the initialization, whose accuracy depends on δ_i. We use a grid spacing of $2\xi/100$ for TO and $2\pi/100$ for PO, thus searching over a 100×100 grid. The size of the grid can be reduced or increased depending on computational resources. As a result, we obtain estimates of the TO, $\hat{\tau}_{o,i}$, and PO, $\hat{\phi}_{o,i}$. Fig. 4b shows an example of the refinement step. The initialization of the TO allows restricting the search to a small area in the cost function that presents a clear minimum.

TO and PO compensation. The TO and PO are compensated for in each subband by applying the phase-rotation and re-modulation steps (see points (i) and (ii) in the problem formulation) using the estimates $\hat{\tau}_{o,i}$, and $\hat{\phi}_{o,i}$. This is mathematically expressed as

$$\bar{H}_{i,s,\kappa} = e^{-j\hat{\phi}_{o,i}} e^{j2\pi\hat{\tau}_{o,i}\kappa\Delta_f} H_{i,s,\kappa}, \tag{5}$$

where the resulting CFR for subband s of subsystem i, $\bar{H}_{i,s,\kappa}$, is now phase-coherent with the reference subsystem, up to estimation errors. This enables the coherent combination of the subbands across the full band of interest.

Remark. The proposed method can handle CFR estimates obtained at different time instants by the different subsystems, as long as the time difference among the estimates is short enough to consider the channel parameters to be constant. To see this, consider Eq. (2) and two CFR estimates obtained by subsystems 1 and 2 at times t_1 and t_2, respectively. If the two estimates are sufficiently close in time, the channel parameters α_l and τ_l can be considered constant. Conversely, the offsets $\tau_{o,2}(t), \phi_{o,2}(t)$ are fast time-varying, so they change from t_1 to t_2. Taking subsystem 1 *at time* t_1, our approach compensates for the cumulative TO and PO, given by $\tau_{o,2}(t_2) + \tau_{o,2}(t_1)$ and $\phi_{o,2}(t_2) + \phi_{o,2}(t_1)$. HiSAC is therefore general enough to handle relative TO and PO due to collecting CFR at different time instants. This feature makes it extremely flexible in utilizing the CFR estimates obtained by the communication system. Moreover, compared to methods based on linear fitting of the unwrapped phase at different subcarriers, e.g., [18, 57], our approach is more effective with non-contiguous frequency bands (see Section 6).

4.3 Multiband fusion

Once the available subbands have been made mutually coherent, we use OMP to obtain a combined set of delay estimates. This step is similar to the intra-subsystem CFR reconstruction in Section 4.1. However, the search space is huge since the number of subcarriers in the full band is much larger than that in the single subsystems, i.e., $K \gg K_i$. Hence, a direct application of OMP would either have prohibitive computational complexity if we select a small grid spacing, or give inaccurate results if the grid spacing is too large. To solve this issue, we leverage the knowledge of the delays estimated by the single subsystems before the coherent fusion to greatly reduce the search space. This can be thought of as focusing the OMP algorithm around the solutions obtained from the lower-resolution subsystems.

Search space reduction. To effectively reduce the search space, we consider the reference subsystem and denote by $\{\tau_{1,1}, \dots, \tau_{1,L_1^{\text{OMP}}}\}$ its set of delays. Instead of considering a complete grid of delays, as done in the intra-subsystem CFR reconstruction, here HiSAC works on a union of discrete intervals around the reference subsystem's solutions. To do so, we first obtain a continuous union of intervals around the candidate delays from the reference subsystem, i.e., $\mathcal{R} = \bigcup_l \mathcal{R}_l$, where $\mathcal{R}_l = [\tau_{1,l} - \gamma, \tau_{1,l} + \gamma]$. γ is the one-sided width of the interval and it is chosen as half the worst nominal delay resolution among the subsystems, i.e., $\gamma = 1/(2\min_i(B_i))$. This way, the search area around the subsystem's solution is conservatively adapted to the subsystem with the lowest resolution.

Then, HiSAC discretizes $\mathcal{R}$ to construct a grid of Q candidate delays for OMP with step δ. The latter determines the final HiSAC delay resolution and accuracy. The elements of the discretized set of delays are denoted by $\nu_1, \dots, \nu_Q$.

Thanks to the search space reduction step, the dimensionality of the problem is reduced from having K candidates to Q candidates. Q can be significantly smaller than K, since L_1^{OMP} is small due to the sparsity of the channel and δ is under our control.

OMP-based solution. Similar to Section 4.1, the subsystem combination can be cast as a compressed sensing problem that we solve using OMP. To this end, we construct a matrix with the candidate complex sinusoidal components in the channel as its columns. This is a *partial* $K \times Q$ Fourier matrix, $\mathbf{F}$, that only contains the candidates corresponding to the delays in set $\{\nu_1, \dots, \nu_Q\}$. The components of $\mathbf{F}$ are defined as $(\mathbf{F})_{k,q} = e^{j2\pi k\nu_q\Delta_f}/\sqrt{K}$. To model the missing subcarrier measurements, we introduce a selector matrix, $\mathbf{A} \in \{0,1\}^{M\times K}$, whose rows are the K-dimensional vectors of all zeros but the k-th component, and each row has a different $k \in \{k_{1,1}, \dots, K_{1,1}-1, \dots, k_{C,S}, \dots, K_{C,S}-1\}$. Left-multiplying $\mathbf{A}$ by $\mathbf{F}$ selects the rows of $\mathbf{F}$ whose indices are in the set of available CFR samples. Call $\boldsymbol{\Gamma} = \mathbf{A}\mathbf{F} \in \mathbb{C}^{M \times Q}$, and define the CFR vector of dimension M

$$\bar{\mathbf{H}} = [\bar{H}_{1,1,0}, \dots, \bar{H}_{1,1,K_1}, \dots, \bar{H}_{C,S,0}, \dots, \bar{H}_{C,S,K_S}]^{\mathsf{T}}, \tag{6}$$

that contains all the available measurements from all the S subbands after TO and PO compensation. We denote by $\mathbf{h} \in \mathbb{C}^Q$ the CIR obtained by fusing the S subbands. Using OMP we estimate $\mathbf{h}$ by solving the same problem in Eq. (3), using $\bar{\mathbf{H}}$ as the measurement vector and $\boldsymbol{\Gamma}$ as the model matrix. As for the single subsystems, OMP is stopped once the reconstruction error with respect to the measurements reaches a 5% threshold, and the corresponding number of non-zero components of $\hat{\mathbf{h}}$ is L^{OMP}. The set of path delays and amplitudes obtained from the non-zero components of $\hat{\mathbf{h}}$ is $\{\hat{\alpha}_l, \hat{\tau}_l\}, l = 1, \dots, L^{\text{OMP}}$. The delays are then mapped to relative distances as $\hat{r}_l = c\hat{\tau}_l - D$, where D is the distance between the TX and the RX, assumed known. Relative distances can be used to localize a target in both mono-static and bi-static scenarios, as described, e.g., in [20, 36, 37].

4.4 Temporal aggregation

In this section, we discuss how HiSAC can improve its ranging accuracy and resolution by aggregating multiple channel estimates across time, as detailed in Alg. 1.

Consider a sequence of N path delays, $\{\hat{\tau}_1(t_n), \dots, \hat{\tau}_{L^{\text{OMP}}}(t_n)\}$, and amplitudes, $\{\hat{\alpha}_1(t_n), \dots, \hat{\alpha}_{L^{\text{OMP}}}(t_n)\}$, for $n = 1, \dots, N$, obtained by applying HiSAC to different ISAC packets or OFDM slots at time instants $t_1, \dots, t_N$. These must be obtained in a short processing interval such that the channel parameters can be considered constant, i.e., $t_N - t_1$ should be within the coherence time of the channel.

Recall that the delays outputted by OMP belong to a discrete grid of candidates ν_q, with $q = 1, \dots, Q$, which is kept fixed during the aggregation period. The temporal aggregation step is based on the following observation: When applied within the coherence time of the channel, HiSAC outputs correlated sets of delays that can be aggregated (coherently or incoherently). To do so, Alg. 1 iterates over the elements in the delay grid and over time slots (lines 2-3). Then, if ν_q is among the set of outputs of OMP in the considered slot n, we accumulate it across time using a running average of the path amplitudes, χ_q (lines 4-6), that combines the current amplitude $\hat{\alpha}_l(t_n)$ with the previous χ_q.

We propose two alternative versions of the running average, one for static targets and one for human sensing (line 5), respectively:

- If the targets are static, the temporal aggregation can be performed by taking into account the phase of the complex amplitudes (coherent aggregation), which gives higher Signal-to-Noise Ratio (SNR) and resolution. This corresponds to the first case in line 5 of Alg. 1.
- With dynamic targets such as humans, instead, we only aggregate the magnitude information for each path (incoherent aggregation) since the time variation of the phase due to respiration or slight movement would lead to destructive interference. This corresponds to the second case in line 5.

Algorithm 1 HiSAC multipath temporal aggregation.

Input: Set of delays and amplitudes across time $\hat{\tau}_l(t_n), \hat{\alpha}_l(t_n)$, for $l = 1, \dots, L^{\text{OMP}}$ and $n = 1, \dots, N$, OMP grid $\nu_1, \dots, \nu_Q$, order L^{OMP}.
Output: Improved set of delays and amplitudes $\{\bar{\alpha}_l, \bar{\tau}_l\}, l = 1, \dots, L^{\text{OMP}}$.
1: Initialize $q = 1$, $\chi_q = 0, \forall q = 1, \dots, Q$.
2: **for** $q = 1, \dots, Q$ **do**
3: **for** $n = 1, \dots, N$ **do**
4: **if** $\nu_q \in \{\hat{\tau}_l(t_n)\}, l = 1, \dots, L^{\text{OMP}}$ **then**
5: $\chi_q \leftarrow \begin{cases} \left[\hat{\alpha}_l(t_n) + n\chi_q\right]/(n+1) & \text{if target is static,} \\ \left[|\hat{\alpha}_l(t_n)| + n\chi_q\right]/(n+1) & \text{otherwise.} \end{cases}$
6: **end if**
7: **end for**
8: **end for**
9: Return $\{\bar{\alpha}_l, \bar{\tau}_l\}, l = 1, \dots, L^{\text{OMP}}$ as the L^{OMP} path delays with the highest χ_q.

Finally, in line 9, we select as the final improved set of delays the L^{OMP} candidates for which χ_q is highest, which we denote by $\bar{\tau}_l$, for $l = 1, \dots, L^{\text{OMP}}$. The channel gains of such delays are the corresponding χ_q, which we call $\bar{\alpha}_l$. The delays are then mapped to relative distances as $\bar{r}_l = c(\bar{\tau}_l - \bar{\tau}_1)$.

5 IMPLEMENTATION

To implement HiSAC, we use the open-source Mimorph platform [22] as a baseline. The platform includes an AMD (Xilinx) RFSoC that comprises Field Programmable Gate Array (FPGA) logic, multiple analog-to-digital/digital-to-analog converters, and ARM processors. We implement HiSAC to work in the unlicensed 58-64 GHz mmWave band using linear antenna array front-ends with 16 elements from Sivers Semiconductors, suitable for analog beamforming. We choose a mmWave frequency band as it represents a challenging test case, given the high sensitivity to CFO and the strong phase noise of high frequencies [40]. Signal conditioning from the RFSoC to the mmWave front-ends includes DC-block filters, low-pass filters (1 GHz cut-off frequency), and 3 dB attenuators. The main components of a TX-RX node of the testbed are shown in Fig. 5a. We configure the testbed to work as $C = 2$ incoherent subsystems with carrier frequencies 60.48 GHz and 62.64 GHz. The testbed can operate concurrently as TX and RX, in mono-static configuration, or as a bi-static system, using two nodes like the one in Fig. 5a.

Signal generation. Signals for each sub-system are generated offline. Evaluating HiSAC requires collecting full band CFR estimates and other information used as ground truth, as detailed in Section 6.1. Therefore, we generate a composite packet including 5G-NR OFDM symbols and IEEE 802.11ay channel estimation fields. An OFDM symbol including De-Modulation-Reference Signal (DM-RS), spanning the full bandwidth, is used as ground truth (see the *Full band* baseline in Section 6.1). An IEEE 802.11ay channel estimation field is used for SC CIR estimation. 5G-NR pilot signals spanning different subbands are used for HiSAC, with bandwidth and starting frequency depending on the specific experiment. The signal is sent to the RFSoC using an Ethernet port and stored in loopback memories implemented in the FPGA logic. The FPGA clock is set to 245.76 MHz with a super-sampling rate factor of 8, giving an equivalent of 1966.08 MHz. The inter-packet time is configurable in runtime by a host PC. Since more than one subsystem is employed, independent data paths are used and connected to independent mmWave front-ends (Fig. 5a).

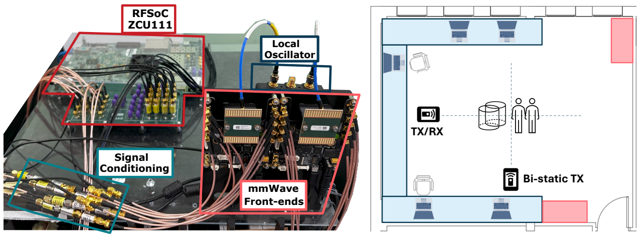

(a) (b)

Figure 5: HiSAC prototype (a) and experimental environment (b).

Signal capture and saving. To enable the testbed operation in mono-/bi-static operation, we modify the packet detection block from [21] to either trigger packet capture when detecting a valid preamble in bi-static operation mode or trigger the capture when transmitting a packet (mono-static mode). The operating mode can be updated at runtime from a host PC. Valid packets are stored in on-board RAM (up to 4GB) and then these are offloaded through a 10 Gb Ethernet interface to be processed offline.

6 EXPERIMENTAL RESULTS

In this section, we describe the experimental setup used in the evaluation of HiSAC. Then we provide an in-depth analysis of our results obtained in different settings.

6.1 Experiments and baselines

Experiments description. To evaluate HiSAC, we perform 27 experiments involving ISAC radio channel measurements in different scenarios and configurations. Each experiment is repeated 5 times and involves the transmission of 100 packets with an inter-packet time of 50 ms (unless stated otherwise). The experiments are carried out indoors, in a 7 m $\times$ 6 m room (see Fig. 5b), and can be divided into six groups detailed in the following. In groups (1)-(5) we use metal cylindric reflectors as targets, while group (6) involves human subjects. Groups (1)-(4) and (6) are obtained in a mono-static scenario, while in (5) we use a bi-static setting. In our experiments, we point the TX beam pattern toward the targets, unless stated otherwise. In practice, algorithms such as the one in [36, 37] can be used to estimate the angular location of the scatterers. As an anchor path to achieve phase coherence, we use the self-interference path in the mono-static scenario and the LOS in the bi-static one.

(1) 2 targets (8 experiments): 2 metal cylinders are placed at different distances from the system, ranging from 1.5 to 5 m. The inter-target distance is changed from 30 cm to 60 cm.

(2) 3 targets (5 experiments): 3 metal cylinders are placed at different distances from the system, ranging from 2 to 5 m. The inter-target distance is changed from 30 cm to 60 cm.

(3) Resolution limit test (3 experiments): 2 metal cylinders are placed at 17.2, 10.1, and 3.1 cm inter-target distance, to evaluate the maximum resolution achieved by HiSAC. The distance of the second target from the TX is 2.78 m.

(4) Changing angle (5 experiments): 2 metal cylinders are placed about 2.5 m from the TX with 33 cm inter-target distance. We change the angular location of the targets in different experiments among $-30°, -15°, 17°, 30°$. In each, experiment, we change the antenna beam pattern used by the TX to point at the targets. This scenario is of high practical interest since pilot signals in ISAC systems (e.g. SSBs) are often beamformed in different directions.

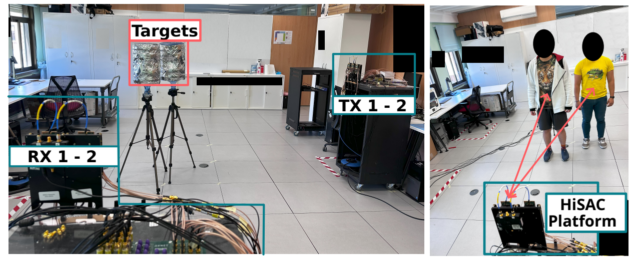

(a) Bi-static setup of subsystems 1 and 2. **(b) Human sensing.**

Figure 6: Experiments in the bi-static setting and with static subjects.

(5) Bi-static scenario: This group of experiments is performed in a bi-static scenario with a distance of 3.24 m between the TX and the RX. 2 metal cylinders are placed close to each other so that the segments connecting the TX to the target, and the target to the RX form a $90°$ angle (bi-static angle). The inter-target bi-static distance changes in different experiments from 3.5 cm to 8.9 cm. This scenario is particularly challenging since the nominal ranging resolution in the bi-static case is degraded by a factor of 0.7 due to the $90°$ bi-static angle, as shown in Section 2.2.

(6) Human localization and tracking: A final group of experiments is performed with human targets, to demonstrate the effectiveness of HiSAC on weaker multipath components with respect to metal reflectors and its robustness to movement. These involve (i) 2 static subjects standing at 2.30 and 2.64 m from the TX as shown in Fig. 6b, (ii) 2 moving targets walking back and forth from 3 to 1 m from the TX (in this case, the inter-packet time is reduced to 5 ms). Experiments involving people have been carried out in compliance with the IRB of our institute and do not disclose information about the subjects.

Baselines for comparison. Since HiSAC is the first method to perform multiband ISAC, we design the baseline methods described in the following. Note that [24], which is the closest prior work, is not suitable for comparison since (i) it is based on a deep neural network trained on sub-6 GHz signals so that it would need extensive data collection and retraining on our implementation, (ii) it uses a channel hopping scheme to collect CFR samples that is specific to sub-6 GHz Wi-Fi and does not apply to 5G-NR.

Laser telemeter. We collect ground truth distance measurements of the targets using a laser telemeter, mounted on the TX-RX antenna front-end.

Full band. We collect CFR measurements over an equivalent bandwidth to the full band of interest and use OMP to obtain target distance estimates. This is a benchmark to assess how close HiSAC gets to the performance of a wideband ISAC system with a bandwidth equal to its total virtual bandwidth.

Contiguous band. We collect CFR measurements over a *contiguous* region of the spectrum with a bandwidth equal to the real bandwidth of HiSAC, which includes only the subcarriers in which

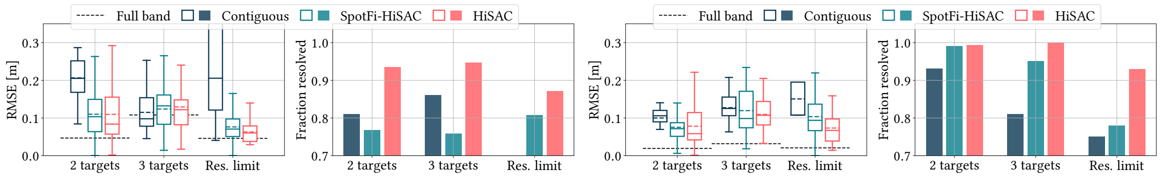

(a) CA-C1. **(b) CA-C2.**

Figure 7: HiSAC results in the CA-C1/C2 setting. We report the ranging RMSE and the FRT in experiment groups (1)-(3).

the channel is measured. OMP is then used to obtain distance estimates.

SpotFi-based HiSAC (SpotFi-HiSAC). To demonstrate the effectiveness of HiSAC's algorithm to achieve phase coherence across subbands, we design a competitor algorithm that uses SpotFi's approach, [18], to perform this task. SpotFi first extracts the phase of the CFR in each subband, representing it as a function of the subcarriers, and applies phase unwrapping to remove the wrapping around 2π. Due to the linearity of the phase as a function of path delays, as can be seen from Eq. (1), a linear model can be fit to the unwrapped CFR of each subband. Then, the phase offsets are removed by applying a linear transformation to the phase of the CFRs. The parameters of the transformation are obtained by matching the slopes and intercepts of the linear models across subbands.

To fairly compare the effectiveness of the phase offsets compensation algorithm, we keep the rest of the delay estimation process the same as in HiSAC. This step is necessary since the original SpotFi uses the MUSIC algorithm to estimate delays, it can not handle non-contiguous subbands. Hence, SpotFi-HiSAC is an *improvement* of the original SpotFi that can be applied to non-contiguous subbands. Specifically, SpotFi-HiSAC applies, in order: the intra-subsystem OMP-based reconstruction from Section 4.1, the SpotFi phase offsets removal step, based on line fitting, and the multiband fusion step from Section 4.3.

Evaluation metrics. We adopt two main metrics to evaluate HiSAC. The first one is the Root Mean Squared Error (RMSE) in the distance estimation, computed with respect to the laser telemeter distance measurement. RMSE can only be computed for the targets that are detected by the algorithm, and it is undefined for unresolved targets. Therefore, we introduce a second metric which we call Fraction of Resolved Targets (FRT). This represents the fraction of targets that an algorithm can resolve, i.e., detect correctly, with respect to the total number of targets resolved by the full band baseline. We consider a target to be correctly detected by an algorithm if this outputs a target distance sufficiently close, i.e., closer than the minimum inter-target distance in the experiment, to the laser telemeter ground truth distance for that target. The two metrics should be jointly considered in each evaluation since an algorithm may yield a very low RMSE but have low resolution, which means it is not exploiting the increased bandwidth. Conversely, an algorithm could have high resolution but poor accuracy, giving a high RMSE.

6.2 In-depth evaluation

In this section, we evaluate HiSAC in the three use cases from Section 2.1, using the experiments from Section 6.1.

Carrier Aggregation. We start our evaluation with the carrier aggregation scenario, combining multiple 5G-NR channels with 100 and 400 MHz bandwidth. We assume that in this case the CFR is estimated over the full channels, similar to using DM-RS pilots that span the full bandwidth [47]. We consider two configurations with 2 subsystems:

(i) Configuration 1 (CA-C1), including 4 subbands with an effective bandwidth of 400 MHz and a virtual bandwidth of 2.01 GHz. The first two subbands belong to subsystem 1, while the second two to subsystem 2. The starting frequencies of the subbands relative to the first one are $\{0, 0.19, 1.63, 1.91\}$ GHz, while their bandwidths are all equal to 100 MHz;

(ii) Configuration 2 (CA-C2), including 5 subbands with an effective bandwidth of 800 MHz and a virtual bandwidth of 3.46 GHz. The first three subbands belong to subsystem 1, while the second two to subsystem 2. The starting frequencies of the subbands relative to the first one are $\{0, 0.19, 1.2, 2.88, 3.36\}$ GHz, while their bandwidths are $\{0.1, 0.1, 0.4, 0.1, 0.1\}$ GHz.

The main challenge in the carrier aggregation scenario is to effectively combine subbands that are widely separated in the spectrum. Fig. 7 shows the RMSE and FRT obtained by HiSAC in experiment groups (1)-(3) with the carrier aggregation use case. The horizontal dashed line represents the average RMSE obtained using the full band CFR. With CA-C1, HiSAC achieves accurate ranging with an average RMSE below 15 cm in all the experiments. The case with 3 targets gives the highest average RMSE due to the higher complexity of the multipath environment. The contiguous bandwidth and SpotFi-HiSAC yield comparable or worse RMSE. This proves that HiSAC gains ranging accuracy thanks to the increased virtual bandwidth and outperforms SpotFi's method to achieve phase coherence. In terms of FRT, HiSAC provides significant gains. In the resolution limit test, the contiguous band is unable to resolve the targets (0.5 FRT), while HiSAC gives 0.93 FRT. With CA-C2, the overall performance in terms of RMSE and FRT on 2 and 3 targets improves for all methods due to the wider virtual bandwidth. However, only HiSAC significantly benefits from such increased virtual bandwidth when considering the resolution limit test, achieving higher FRT compared to CA-C1, while other methods perform slightly worse.

Bandwidth Part. Next, we analyze a bandwidth part scenario, where we combine multiple CFR estimates obtained by a 5G-NR system using SSB signals, spanning 240 subcarriers in the middle of the operating channel. Note that here the bandwidth of each subband is significantly lower than in the carrier aggregation case since the CFR is measured only on a fraction of the total communication channel. Specifically, using 240 KHz subcarrier spacing, which is reasonable at mmWave frequencies, the bandwidth of each

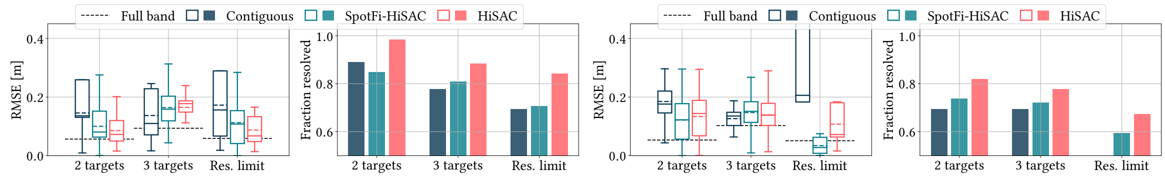

(a) BWP-C1. **(b) BWP-C2.**

Figure 8: HiSAC results in the BWP-C1/C2 setting. We report the ranging RMSE and the FRT in experiment groups (1)-(3).

SSB is $B_{i,s} = 57.6$ MHz. We consider two different configurations with 2 subsystems:

(i) Configuration 1 (BWP-C1), including 4 subbands with an effective bandwidth of 460.8 MHz and a virtual bandwidth of 1.267 GHz. The first four subbands belong to subsystem 1, while the second four to subsystem 2. The starting frequencies of the subbands relative to f_0 are $\{0.02, 0.12, 0.22, 0.32, 0.91, 1.01, 1.11, 1.21\}$ GHz;

(ii) Configuration 2 (BWP-C2), including 5 subbands with an effective bandwidth of 230.4 MHz and a virtual bandwidth of 1.267 GHz. The first two subbands belong to subsystem 1, while the second two to subsystem 2. The starting frequencies of the subbands relative to the start of the full band are $\{0.02, 0.12, 0.91, 1.01\}$ GHz.

We stress that, as required by bandwidth part operation, each channel estimate in different subbands is obtained at a different time instant, with an inter-packet time of 50 ms. Hence, the spectrum occupied at each time instant is just 57.6 MHz. An example result on BWP-C1 is shown in Fig. 9, reporting the CFR (above) and the squared magnitude of the CIR (below). The main challenge in the bandwidth part scenario is to combine narrow available subbands due to the use of unmodified SSB pilot signals. Fig. 8 shows the RMSE and FRT obtained by HiSAC in the experiment groups (1)-(3) with the bandwidth part use case. With BWP-C1, HiSAC outperforms the other approaches. Note that with 3 targets it achieves a slightly higher mean ranging error with respect to the contiguous band (2 cm), but resolves a higher fraction of targets by 0.1. BWP-C2 represents a very challenging scenario due to the sparsity of the available spectrum (amounting to 18% of the virtual bandwidth) and to the narrow subbands used. In the resolution limit test, the contiguous CFR method fails in resolving the targets and has a large ranging error, while HiSAC achieves 11 cm average error and resolves 67% of the targets on average, with a resolution gain of 13% over SpotFi-HiSAC.

Cross-technology evaluation. To demonstrate the flexibility of HiSAC, we evaluate it in a cross-technology scenario where we combine a 400 MHz 5G-NR OFDM channel, with carrier frequency 59.69 GHz, with a 1.76 GHz IEEE 802.11ay SC channel (WiGig) with carrier frequency 62.64 GHz. The virtual bandwidth in this configuration is 4.03 GHz, while the available one is 2.16 GHz. Note that, in SC systems, the CIR is estimated directly via cross-correlation with the transmitted pilot signals. Therefore, before applying HiSAC, we convert the IEEE 802.11ay CIR into the CFR using a DFT. In Fig. 10, we show the RMSE and FRT results in the cross-technology scenario. As a comparison, we use the targets detected by the peaks of the CIR estimated by a single IEEE 802.11ay channel. HiSAC obtains extremely accurate ranging with an average RMSE of at most 5 cm (3 targets), whereas the single channel has a

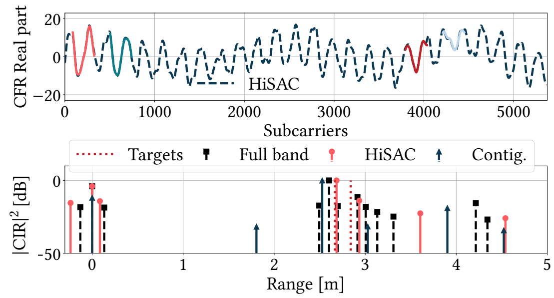

Figure 9: Example HiSAC results in BWP-C2. The top plot shows the subbands after coherency has been achieved and the reconstructed HiSAC CFR. The bottom plot shows the CIR squared magnitude.

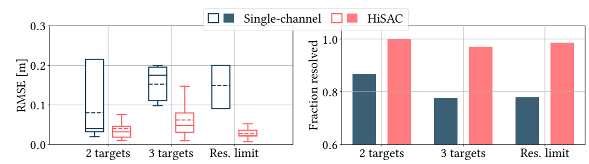

Figure 10: Cross-technology HiSAC results.

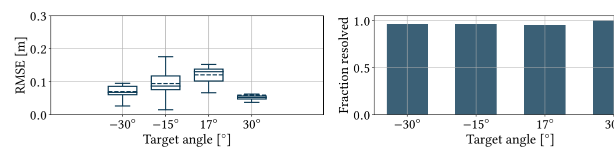

Figure 11: HiSAC results changing target angle and transmission beam pattern.

worst-case RMSE of 15 cm. In terms of FRT, HiSAC gives an almost identical resolution to the full bandwidth, with a worst-case FRT of 0.95 with three targets.

Impact of angle and beamforming. ISAC systems apply beamforming to direct the signal towards the communication RX or targets. HiSAC is robust to such changes in the direction of the transmission, as demonstrated by our results in Fig. 11, obtained on experiments group (4). The ranging RMSE remains below 15 cm when changing the angle in $[-30°, 30°]$. The FRT does not change significantly when changing the transmission angle, proving that HiSAC accurately measures distances in different directions.

Bi-static setting. We evaluate HiSAC's capability to estimate the targets' distances in a bi-static setting, using experiments from group (5) and the BWP-C1/C2 configurations. Note that the full band range resolution in this case is reduced to $\Delta r = c/(2B\cos(\pi/4))$

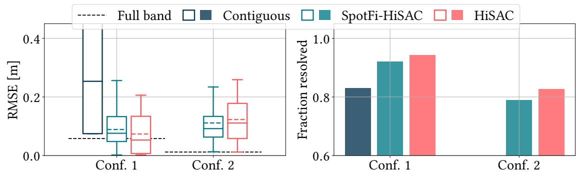

Figure 12: HiSAC results in a bi-static bandwidth part scenario.

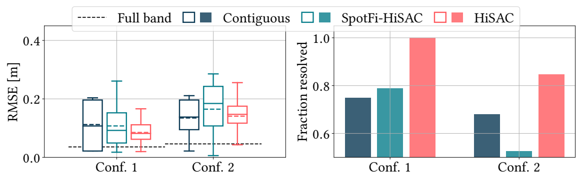

Figure 13: HiSAC results with human subjects using bandwidth part.

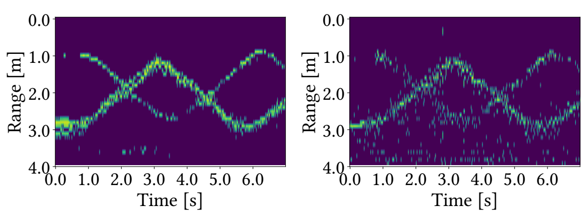

Figure 14: Tracking 2 subjects across time in the BWP-C1 scenario. We plot the normalized CIR squared magnitude obtained from the reconstructed CIR with the full band (left) and HiSAC (right). HiSAC's resolution is comparable to that of the full 1.2 GHz bandwidth.

$\approx$ 17.5 cm due to the bi-static angle being 90°. Fig. 12 shows the RMSE and FRT obtained by HiSAC in the bi-static setting. These results are comparable to those obtained in the mono-static setting with a similar configuration, proving that HiSAC works when the TX and RX are widely separated. Conversely, the contiguous CFR can not resolve the targets with BWP-C2.

People localization. We test HiSAC on human subjects to demonstrate its capability to resolve weaker reflections, using the experiments from group (6). Fig. 13 shows the RMSE and the FRT. These results are obtained using the BWP-C1 and C2 configurations. HiSAC achieves 8 and 15 cm average RMSE with C1 and C2, respectively. Moreover, the FRT gain that it provides with respect to using the contiguous CFR is large: 0.25 using C1 and 0.17 using C2. Note that SpotFi-HiSAC's FRT with human subjects degrades much more than HiSAC's. Being based on an anchor path, our method to achieve phase coherence is *independent* of the strength of the target multipath component.

People tracking. Fig. 14 shows the CIR squared magnitude across time obtained from the CIR estimated by HiSAC and with the full band with 2 subjects walking back and forth. Peaks in the CIR (in yellow) correspond to the subjects. Although HiSAC's CIR is noisier than that of the full band, its resolution, i.e., the capability of distinguishing the two subjects across time, is comparable. The bandwidth used by HiSAC in each time slot is only 57.6 MHz (20 times lower than the full bandwidth), i.e., 2.6 m resolution.

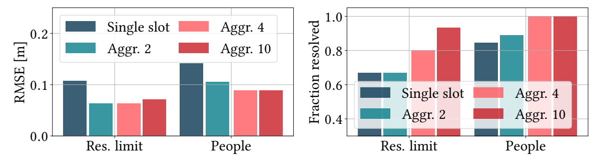

Figure 15: Improvement due to the temporal aggregation (Alg. 1) on experiments (3), Resolution limit, and (6), People, using BWP-C2.

Temporal aggregation improvement. Fig. 15 shows the RMSE and FRT results obtained by aggregating HiSAC's range estimates over 2, 4, or 10 time slots using Alg. 1. This evaluation is carried out on the most challenging scenarios we considered during the evaluation, namely BWP-C2 and groups of experiments (3) and (6). Our results demonstrate the effectiveness of temporal aggregation, which improves RMSE by around 30% and FRT by up to 0.25 with respect to single-slot HiSAC.

7 RELATED WORK

Super-resolution wireless sensing. Subspace-based super-resolution methods [19] and compressed sensing [10] are widely used in radar and ISAC, but are still limited by the transmission bandwidth. Some of their recent applications to ISAC are found in [28, 63]. Other approaches have employed the spatial diversity of the RX array [65] to perform high-resolution imaging in the mmWave band, but they can not be applied to low-cost systems with a single RF chain such as analog beamforming systems. In [31, 44], a novel approach is introduced to apply distributed Synthetic Aperture Radar (SAR) techniques to vehicular sensing systems. This approach boosts the resolution by combining distributed devices, thus requiring multiple cooperating nodes. HiSAC instead *reuses* the frequency diversity of communication systems without additional requirements. Notably, HiSAC could be combined with any of the above techniques to enhance their resolution.

Multiband radar sensing. Multiband sensing has been studied in the radar literature. [8] has first proposed bandwidth interpolation between two subbands to increase ranging resolution via Auto-Regressive (AR) modeling and non-linear optimization. Other works have followed a similar research direction adopting different algorithms for combining the subbands [11, 13, 46, 48, 56, 66, 69]. The above works are based on radar systems with optimized chirp waveforms using wide individual subbands. This significantly simplifies the problem with respect to an ISAC setting where CFR estimates are not under control and can be very narrow, making radar approaches underperform. To solve this problem, HiSAC innovates with a progressive combination of subbands over coherent subsystems first, and then over the full band of interest.

OFDM-based multiband processing. Several works have demonstrated that combining multiple frequency bands can boost the resolution of OFDM systems in active localization. In [18, 55, 57], SpotFi, Splicer, and ToneTrack are presented, which combine (*stitch*) multiple contiguous or overlapping Wi-Fi subbands to increase the multipath resolution. They use linear fitting of the unwrapped phase to eliminate phase offsets, which leads to errors when used on non-contiguous, narrow subbands spanning several GHz. Other Wi-Fi-based approaches [16, 17, 49] have tackled the same problem but rely on a handshaking process between TX and RX to eliminate phase offsets, which does not apply to passive sensing in ISAC. Similarly, also the frequency hopping strategies used in [3, 6] require the cooperation of the receiver node, which may not be available in ISAC. [15, 35, 51, 52] propose alternative algorithms based on maximum-likelihood. All these approaches target active localization, in which the RX device is the localized target. HiSAC instead localizes targets from backscattered reflections, as done by radars.

More recently, [50] has brought the research attention to exploiting multiband CFR to perform wideband radar-like ranging in ISAC. To the best of our knowledge, the only system that tackles this problem is UWB-Fi [24], in the sub-6 GHz unlicensed spectrum. However, this system is based on a neural network that learns to combine subbands and compensate for phase offsets. Changing hardware, frequency band, or technology (OFDM vs SC) may require retraining the system which is time-consuming and requires new data. Conversely, HiSAC does not require training and generalizes to different implementations.

Cross-band channel prediction. A recent line of work has investigated channel prediction in one frequency band from an available channel estimate in a different band [1, 2, 7, 23, 29, 43]. This is typically done to avoid having to transmit feedback channel information in downlink/uplink, thus reducing overhead. Although the general idea of this problem is linked to the multiband setting, predicting the channel in a different band is significantly different from combining multiple non-contiguous incoherent CFR estimates to increase the total system bandwidth. Moreover, the above works focus on communication, hence the channel prediction is mostly aimed at estimating SNR at the RX. Conversely, HiSAC is an ISAC system that estimates fine-grained complex amplitudes and delays of individual paths in the channel.

8 DISCUSSION AND LIMITATIONS

Sensing over very large bandwidth. HiSAC can aggregate subbands over regions of the spectrum spanning several GHz. However, aggregation between very far frequency bands (e.g., sub-6 GHz and mmWave) is not feasible, since the frequency-dependency of the scattering coefficients of the different paths would become non-negligible and prevent coherent aggregation. Future research in this direction is key to truly exploit the multiband potential.

Impact of the scattering angle. The phase of the scattering coefficients $\alpha_l(t)$ in Eq. (2) is assumed to be approximately constant for all subsystems. This assumption holds for isotropic targets or if the scattering angle is similar across subsystems [31]. This assumption is reasonable for ISAC BSs and APs that are typically clustered on the same antenna poles. Combining spatially diverse subsystems across multiple bands will be investigated in future work.

Impact of narrow subbands. In the limit case in which each HiSAC subsystem estimates a single very narrow subband, reconstructing a subsystem-wide CFR model could be challenging. If targets are too close to the TX, the CFR may not oscillate fast enough to have sufficient information about the path delay in the narrow subband. This is a challenging problem that requires further investigation.

Impact of Doppler. The impact of Doppler on subbands combination remains unexplored in ISAC. Due to its variation with carrier frequency, Doppler introduces a path- and subsystem-specific phase shift on the CFR which may degrade the subbands combination. HiSAC is sufficiently robust to this phenomenon as shown in Section 6.2. However, further investigation of this aspect is required.

9 CONCLUSION

The problem of achieving range super-resolution in ISAC systems with narrow and discontinuous subbands is addressed in this paper. To solve it, we present HiSAC, a general signal-processing method for coherent multiband ranging that enhances the resolution of existing communication systems by only reusing channel estimates obtained via pilot signals. Our approach does not rely on specific hardware or protocol and works across different communication technologies (i.e., 5G-NR or IEEE 802.11ay). Our extensive experiments with objects and humans demonstrate that HiSAC enhances the resolution by up to 20 times compared to single-band processing, occupying the same bandwidth in each time slot.

ACKNOWLEDGMENTS

The work of Jacopo Pegoraro and Michele Rossi was funded by the European Union under the Italian National Recovery and Resilience Plan (NRRP) Mission 4, Component 2, Investment 1.3, CUP C93C22005250001, partnership on "Telecommunications of the Future" (PE00000001 - program "RESTART"). The work of Jesus O. Lacruz and Joerg Widmer has been partially funded by project PID2022-136769NB-I00 funded by MCIN/AEI /10.13039/501100011033 / FEDER, UE, and by project RISC-6G TSI-063000-2021-59, funded by Spanish Ministry of Economic Affairs and Digital Transformation, European Union NextGeneration-EU.

REFERENCES

[1] Arjun Bakshi, Yifan Mao, Kannan Srinivasan, and Srinivasan Parthasarathy. 2019. Fast and Efficient Cross Band Channel Prediction Using Machine Learning. In *The 25th Annual International Conference on Mobile Computing and Networking* (Los Cabos, Mexico) *(MobiCom '19)*. Association for Computing Machinery, New York, NY, USA, Article 37, 16 pages.

[2] Avishek Banerjee, Xingya Zhao, Vishnu Chhabra, Kannan Srinivasan, and Srinivasan Parthasarathy. 2024. HORCRUX: Accurate Cross Band Channel Prediction. In *Proceedings of the 30th Annual International Conference on Mobile Computing and Networking* (Washington D.C., DC, USA) *(ACM MobiCom '24)*. Association for Computing Machinery, New York, NY, USA, 1–15.

[3] Atul Bansal, Akshay Gadre, Vaibhav Singh, Anthony Rowe, Bob Iannucci, and Swarun Kumar. 2021. OwLL: Accurate LoRa Localization using the TV Whitespaces. In *Proceedings of the 20th International Conference on Information Processing in Sensor Networks (Co-Located with CPS-IoT Week 2021)* (Nashville, TN, USA) *(IPSN '21)*. Association for Computing Machinery, New York, NY, USA, 148–162. https://doi.org/10.1145/3412382.3458263

[4] Sergio Barrachina-Muñoz, Boris Bellalta, and Edward W Knightly. 2021. Wi-Fi channel bonding: An all-channel system and experimental study from urban hotspots to a sold-out stadium. *IEEE/ACM Transactions on Networking* 29, 5 (2021), 2101–2114.

[5] Xu Chen, Zhiyong Feng, J Andrew Zhang, Xin Yuan, and Ping Zhang. 2023. Kalman Filter-based Sensing in Communication Systems with Clock Asynchronism. *IEEE Transactions on Communications* (2023).

[6] Zhe Chen, Guorong Zhu, Sulei Wang, Yuedong Xu, Jie Xiong, Jin Zhao, Jun Luo, and Xin Wang. 2021. M^3: Multipath Assisted Wi-Fi Localization with a Single Access Point. *IEEE Transactions on Mobile Computing* 20, 2 (2021), 588–602. https://doi.org/10.1109/TMC.2019.2950315

[7] Kun Woo Cho, Marco Cominelli, Francesco Gringoli, Joerg Widmer, and Kyle Jamieson. 2023. Scalable Multi-Modal Learning for Cross-Link Channel Prediction in Massive IoT Networks *(MobiHoc '23)*. Association for Computing Machinery, New York, NY, USA, 221–229. https://doi.org/10.1145/3565287.3610280

[8] Kevin M Cuomo, Jean E Pion, and Joseph T Mayhan. 1999. Ultrawide-band coherent processing. *IEEE Transactions on Antennas and Propagation* 47, 6 (1999), 1094–1107.

[9] Anastasia Daraseliya, Maksym Korshykov, Eduard Sopin, Dmitri Moltchanov, Sergey Andreev, and Konstantin Samouylov. 2021. Coexistence Analysis of 5G NR Unlicensed and WiGig in Millimeter-Wave Spectrum. *IEEE Transactions on Vehicular Technology* 70, 11 (2021), 11721–11735.

[10] Yonina C Eldar and Gitta Kutyniok. 2012. *Compressed sensing: theory and applications.* Cambridge University Press.

[11] Bilal Hussain, Antonio Malacarne, Salvatore Maresca, Filippo Scotti, Paolo Ghelfi, and Antonella Bogoni. 2018. Auto-regressive spectral gap filling algorithms for photonics-based highly sparse coherent multi-band radars in complex scenarios. In *2018 IEEE Radar Conference (RadarConf18)*. IEEE, 0993–0998.

[12] Sijie Ji, Xuanye Zhang, Yuanqing Zheng, and Mo Li. 2024. Construct 3D Hand Skeleton with Commercial WiFi. In *Proceedings of the 21st ACM Conference on Embedded Networked Sensor Systems* (Istanbul, Turkiye) *(SenSys '23)*. Association for Computing Machinery, New York, NY, USA, 322–334.

[13] Li Jia and Xiaojian Xu. 2006. A new procedure for ultra wideband radar imaging from sparse subband data. In *2006 8th international Conference on Signal Processing*, Vol. 4. IEEE.

[14] Wenjun Jiang, Hongfei Xue, Chenglin Miao, Shiyang Wang, Sen Lin, Chong Tian, Srinivasan Murali, Haochen Hu, Zhi Sun, and Lu Su. 2020. Towards 3D human pose construction using wifi. In *Proceedings of the 26th Annual International Conference on Mobile Computing and Networking* (London, United Kingdom) *(MobiCom '20)*. Association for Computing Machinery, New York, NY, USA, Article 23, 14 pages.

[15] Tarik Kazaz, Gerard JM Janssen, Jac Romme, and Alle-Jan Van der Veen. 2021. Delay estimation for ranging and localization using multiband channel state information. *IEEE Transactions on Wireless Communications* 21, 4 (2021), 2591–2607.

[16] Mahdi Barzegar Khalilsarai, Benedikt Gross, Stelios Stefanatos, Gerhard Wunder, and Giuseppe Caire. 2020. WiFi-based channel impulse response estimation and localization via multi-band splicing. In *GLOBECOM 2020-2020 IEEE Global Communications Conference*. IEEE, Taipei, Taiwan.

[17] Mahdi Barzegar Khalilsarai, Stelios Stefanatos, Gerhard Wunder, and Giuseppe Caire. 2019. WiFi-based indoor localization via multi-band splicing and phase retrieval. In *2019 IEEE 20th International Workshop on Signal Processing Advances in Wireless Communications (SPAWC)*. IEEE, Cannes, France.

[18] Manikanta Kotaru, Kiran Joshi, Dinesh Bharadia, and Sachin Katti. 2015. SpotFi: Decimeter Level Localization Using WiFi. *SIGCOMM Comput. Commun. Rev.* 45, 4 (aug 2015), 269–282. https://doi.org/10.1145/2829988.2787487

[19] Sun-Yuan Kung, K Si Arun, and DV Bhaskar Rao. 1983. State-space and singular-value decomposition-based approximation methods for the harmonic retrieval problem. *JOSA* 73, 12 (1983), 1799–1811.

[20] Heiner Kuschel, Diego Cristallini, and Karl Erik Olsen. 2019. Tutorial: Passive radar tutorial. *IEEE Aerospace and Electronic Systems Magazine* 34, 2 (2019), 2–19.

[21] Jesus O. Lacruz, Dolores Garcia, Pablo Jiménez Mateo, Joan Palacios, and Joerg Widmer. 2020. mm-FLEX: An Open Platform for Millimeter-Wave Mobile Full-Bandwidth Experimentation. In *ACM MobiSys'20*.

[22] Jesus O. Lacruz, Rafael Ruiz, and Joerg Widmer. 2021. A Real-Time Experimentation Platform for sub-6 GHz and Millimeter-Wave MIMO Systems. In *ACM MobiSys'21*.

[23] Qianru Li, Zhehui Zhang, Yanbing Liu, Zhaowei Tan, Chunyi Peng, and Songwu Lu. 2023. CA++: Enhancing Carrier Aggregation Beyond 5G. In *Proceedings of the 29th Annual International Conference on Mobile Computing and Networking (MobiCom '23)*. Association for Computing Machinery, New York, NY, USA, Article 5, 14 pages.

[24] Xin Li, Hongbo Wang, Zhe Chen, Zhiping Jiang, and Jun Luo. 2024. UWB-Fi: Pushing Wi-Fi towards Ultra-wideband for Fine-Granularity Sensing. In *Proceedings of the 22nd Annual International Conference on Mobile Systems, Applications and Services* (Minato-ku, Tokyo, Japan) *(MOBISYS '24)*. Association for Computing Machinery, New York, NY, USA, 42–55. https://doi.org/10.1145/3643832.3661889

[25] Xinyu Li, J Andrew Zhang, Kai Wu, Yuanhao Cui, and Xiaojun Jing. 2022. CSI-ratio-based Doppler frequency estimation in integrated sensing and communications. *IEEE Sensors Journal* (2022).

[26] Guiping Lin, Weiwei Jiang, Sicong Xu, Xiaobo Zhou, Xing Guo, Yujun Zhu, and Xin He. 2023. Human Activity Recognition Using Smartphones With WiFi Signals. *IEEE Transactions on Human-Machine Systems* 53, 1 (2023), 142–153.

[27] Xingqin Lin, Dongsheng Yu, and Henning Wiemann. 2021. *A Primer on Bandwidth Parts in 5G New Radio.* Springer International Publishing. https://doi.org/10.1007/978-3-030-58197-8_12

[28] Yongjun Liu, Guisheng Liao, Yufeng Chen, Jingwei Xu, and Yingzeng Yin. 2020. Super-Resolution Range and Velocity Estimations With OFDM Integrated Radar and Communications Waveform. *IEEE Transactions on Vehicular Technology* 69, 10 (2020), 11659–11672.

[29] Zikun Liu, Gagandeep Singh, Chenren Xu, and Deepak Vasisht. 2021. FIRE: enabling reciprocity for FDD MIMO systems. In *Proceedings of the 27th Annual International Conference on Mobile Computing and Networking* (New Orleans, Louisiana) *(MobiCom '21)*. Association for Computing Machinery, New York, NY, USA, 628–641. https://doi.org/10.1145/3447993.3483275

[30] Shihang Lu, Fan Liu, Yunxin Li, Kecheng Zhang, Hongjia Huang, Jiaqi Zou, Xinyu Li, Yuxiang Dong, Fuwang Dong, Jia Zhu, et al. 2024. Integrated sensing and communications: Recent advances and ten open challenges. *IEEE Internet of Things Journal* (2024).

[31] Marco Manzoni, Dario Tagliaferri, Stefano Tebaldini, Marouan Mizmizi, Andrea Virgilio Monti-Guarnieri, Claudio Maria Prati, and Umberto Spagnolini. 2023. Wavefield networked sensing: Principles, algorithms and applications. *arXiv preprint arXiv:2305.10333* (2023).

[32] Francesca Meneghello, Domenico Garlisi, Nicolò Dal Fabbro, Ilenia Tinnirello, and Michele Rossi. 2023. SHARP: Environment and Person Independent Activity Recognition With Commodity IEEE 802.11 Access Points. *IEEE Transactions on Mobile Computing* 22, 10 (2023), 6160–6175. https://doi.org/10.1109/TMC.2022.3185681

[33] Andreas F Molisch. 2009. Ultra-wide-band propagation channels. *Proc. IEEE* 97, 2 (2009), 353–371.

[34] Zhitong Ni, J Andrew Zhang, Xiaojing Huang, Kai Yang, and Jinhong Yuan. 2021. Uplink sensing in perceptive mobile networks with asynchronous transceivers. *IEEE Transactions on Signal Processing* 69 (2021), 1287–1300.

[35] Matteo Noschese, Fulvio Babich, Massimiliano Comisso, and Chris Marshall. 2020. Multi-band time of arrival estimation for long term evolution (LTE) signals. *IEEE Transactions on Mobile Computing* 20, 12 (2020), 3383–3394.

[36] Jacopo Pegoraro, Jesus O. Lacruz, Tommy Azzino, Marco Mezzavilla, Michele Rossi, Joerg Widmer, and Sundeep Rangan. 2024. JUMP: Joint Communication and Sensing With Unsynchronized Transceivers Made Practical. *IEEE Transactions on Wireless Communications* 23, 8 (2024), 9759–9775. https://doi.org/10.1109/TWC.2024.3365853

[37] Jacopo Pegoraro, Jesus O. Lacruz, Francesca Meneghello, Enver Bashirov, Michele Rossi, and Joerg Widmer. 2024. RAPID: Retrofitting IEEE 802.11ay Access Points for Indoor Human Detection and Sensing. *IEEE Transactions on Mobile Computing* 23, 5 (2024), 4501–4519. https://doi.org/10.1109/TMC.2023.3291882

[38] Jacopo Pegoraro, Jesus O. Lacruz, Michele Rossi, and Joerg Widmer. 2022. SPARCS: A Sparse Recovery Approach for Integrated Communication and Human Sensing in mmWave Systems. In *2022 21st ACM/IEEE International Conference on Information Processing in Sensor Networks (IPSN)*. 79–91. https://doi.org/10.1109/IPSN54338.2022.00014

[39] Qualcomm. 2020. *5G unlicensed shared spectrum.* https://www.qualcomm.com/research/5g/5g-unlicensed-shared-spectrum.

[40] Maryam Eslami Rasekh, Mohammed Abdelghany, Upamanyu Madhow, and Mark Rodwell. 2019. Phase noise analysis for mmwave massive MIMO: a design framework for scaling via tiled architectures. In *Conference on Information Sciences and Systems (CISS)*.

[41] Mark A Richards, Jim Scheer, William A Holm, and William L Melvin. 2010. *Principles of modern radar.* Scitech Publishing Inc., Raleigh, NC, USA.

[42] Piotr Samczyński, Karol Abratkiewicz, Marek Płotka, Tomasz P Zieliński, Jacek Wszołek, Sławomir Hausman, Piotr Korbel, and Adam Ksieżyk. 2021. 5G Network-Based Passive Radar. *IEEE Transactions on Geoscience and Remote Sensing* 60 (2021), 1–9.

[43] Clayton Shepard, Hang Yu, Narendra Anand, Erran Li, Thomas Marzetta, Richard Yang, and Lin Zhong. 2012. Argos: practical many-antenna base stations. In *Proceedings of the 18th Annual International Conference on Mobile Computing and Networking* (Istanbul, Turkey) *(Mobicom '12)*. Association for Computing Machinery, New York, NY, USA, 53–64. https://doi.org/10.1145/2348543.2348553

[44] Dario Tagliaferri, Marco Manzoni, Marouan Mizmizi, Stefano Tebaldini, Andrea Virgilio Monti-Guarnieri, Claudio Maria Prati, and Umberto Spagnolini. 2024. Cooperative Coherent Multistatic Imaging and Phase Synchronization in Networked Sensing. *IEEE Journal on Selected Areas in Communications* 42, 10 (2024), 2905–2921. https://doi.org/10.1109/JSAC.2024.3414609

[45] Paolo Testolina, Michele Polese, Josep M. Jornet, Tommaso Melodia, and Michele Zorzi. 2024. Modeling Interference for the Coexistence of 6G Networks and Passive Sensing Systems. *IEEE Transactions on Wireless Communications* (2024), 1–1. https://doi.org/10.1109/TWC.2024.3360628

[46] Jihua Tian, Jinping Sun, Guohua Wang, Yanping Wang, and Weixian Tan. 2013. Multiband radar signal coherent fusion processing with IAA and apFFT. *IEEE Signal Processing Letters* 20, 5 (2013), 463–466.

[47] 3GPP TS38.300. 2018. NR and NG-RAN Overall Description; Stage 2 (Release 15). *V15.2.0 (2018-06)* (2018).

[48] Philip van Dorp, Rob Ebeling, and Albert G Huizing. 2010. High resolution radar imaging using coherent multiband processing techniques. In *2010 IEEE Radar Conference*. IEEE, 981–986.

[49] Deepak Vasisht, Swarun Kumar, and Dina Katabi. 2016. Decimeter-Level localization with a single WiFi access point. In *13th USENIX symposium on networked systems design and implementation (NSDI 16)*. 165–178.

[50] Yubo Wan, Zhixiang Hu, An Liu, Rui Du, Tony Xiao Han, and Tony Q. S. Quek. 2024. OFDM-Based Multiband Sensing For ISAC: Resolution Limit, Algorithm Design, and Open Issues. *IEEE Vehicular Technology Magazine* 19, 2 (2024), 51–59.

[51] Yubo Wan, An Liu, Rui Du, and Tony Xiao Han. 2022. Fundamental Limits and Optimization of Multiband Sensing. *arXiv preprint arXiv:2207.10306* (2022).

[52] Yubo Wan, An Liu, Qiyu Hu, Mianyi Zhang, and Yunlong Cai. 2023. Multiband Delay Estimation for Localization Using a Two-Stage Global Estimation Scheme. *IEEE Transactions on Wireless Communications* 22, 12 (2023), 9263–9277. https://doi.org/10.1109/TWC.2023.3269624

[53] Chenshu Wu, Feng Zhang, Beibei Wang, and KJ Ray Liu. 2020. mmTrack: Passive multi-person localization using commodity millimeter wave radio. In *IEEE INFOCOM 2020-IEEE Conference on Computer Communications*. IEEE, 2400–2409.

[54] Kai Wu, Jacopo Pegoraro, Francesca Meneghello, J Andrew Zhang, Jesus O Lacruz, Joerg Widmer, Francesco Restuccia, Michele Rossi, Xiaojing Huang, Daqing Zhang, et al. 2024. Sensing in Bi-Static ISAC Systems with Clock Asynchronism: A Signal Processing Perspective. *IEEE Signal Processing Magazine* (2024).

[55] Yaxiong Xie, Zhenjiang Li, and Mo Li. 2015. Precise Power Delay Profiling with Commodity WiFi *(MobiCom '15)*. Association for Computing Machinery, New York, NY, USA, 53–64. https://doi.org/10.1145/2789168.2790124

[56] Di Xiong, Junling Wang, Xiaoyang Qi, and Meiguo Gao. 2017. A coherent compensation method for multiband fusion imaging. In *2017 IEEE Radar Conference (RadarConf)*. IEEE, 1024–1027.

[57] Jie Xiong, Karthikeyan Sundaresan, and Kyle Jamieson. 2015. ToneTrack: Leveraging Frequency-Agile Radios for Time-Based Indoor Wireless Localization. In *Proceedings of the 21st Annual International Conference on Mobile Computing and Networking* (Paris, France) *(MobiCom '15)*. Association for Computing Machinery, New York, NY, USA, 537–549.

[58] Xin Yang, Jian Liu, Yingying Chen, Xiaonan Guo, and Yucheng Xie. 2020. MU-ID: Multi-user identification through gaits using millimeter wave radios. In *IEEE INFOCOM 2020-IEEE Conference on Computer Communications*. IEEE, 2589–2598.

[59] Zhiyun Yao, Xuanzhi Wang, Kai Niu, Rong Zheng, Junzhe Wang, and Daqing Zhang. 2024. WiProfile: Unlocking Diffraction Effects for Sub-Centimeter Target Profiling Using Commodity WiFi Devices. In *Proceedings of the 30th Annual International Conference on Mobile Computing and Networking* (Washington D.C., DC, USA) *(ACM MobiCom '24)*. Association for Computing Machinery, New York, NY, USA, 185–199.

[60] Youwei Zeng, Dan Wu, Jie Xiong, Jinyi Liu, Zhaopeng Liu, and Daqing Zhang. 2020. MultiSense: Enabling multi-person respiration sensing with commodity WiFi. *Proceedings of the ACM on Interactive, Mobile, Wearable and Ubiquitous Technologies* 4, 3 (2020), 1–29.

[61] Youwei Zeng, Dan Wu, Jie Xiong, Enze Yi, Ruiyang Gao, and Daqing Zhang. 2019. FarSense: Pushing the range limit of WiFi-based respiration sensing with CSI ratio of two antennas. *Proceedings of the ACM on Interactive, Mobile, Wearable and Ubiquitous Technologies* 3, 3 (2019), 1–26.

[62] Andrew Zhang, Md Lushanur Rahman, Xiaojing Huang, Yingjie Jay Guo, Shanzhi Chen, and Robert W Heath. 2020. Perceptive mobile networks: Cellular networks with radio vision via joint communication and radar sensing. *IEEE Vehicular Technology Magazine* 16, 2 (2020), 20–30.

[63] Chaoyue Zhang, Zhiwen Zhou, Huizhi Wang, and Yong Zeng. 2023. Integrated super-resolution sensing and communication with 5G NR waveform: Signal processing with uneven CPs and experiments. In *2023 21st International Symposium on Modeling and Optimization in Mobile, Ad Hoc, and Wireless Networks (WiOpt)*. IEEE, 681–688.

[64] Fusang Zhang, Zhaoxin Chang, Jie Xiong, and Daqing Zhang. 2021. Exploring LoRa for Sensing. *GetMobile: Mobile Comp. and Comm.* 25, 2 (sep 2021), 33–37. https://doi.org/10.1145/3486880.3486890

[65] Feng Zhang, Chenshu Wu, Beibei Wang, and K. J. Ray Liu. 2021. mmEye: Super-Resolution Millimeter Wave Imaging. *IEEE Internet of Things Journal* 8, 8 (2021), 6995–7008.

[66] Huan Huan Zhang and Ru Shan Chen. 2014. Coherent processing and super-resolution technique of multi-band radar data based on fast sparse Bayesian learning algorithm. *IEEE Transactions on Antennas and Propagation* 62, 12 (2014), 6217–6227.

[67] J Andrew Zhang, Fan Liu, Christos Masouros, Robert W Heath, Zhiyong Feng, Le Zheng, and Athina Petropulu. 2021. An overview of signal processing techniques for joint communication and radar sensing. *IEEE Journal of Selected Topics in Signal Processing* 15, 6 (2021), 1295–1315.

[68] J Andrew Zhang, Kai Wu, Xiaojing Huang, Y Jay Guo, Daqing Zhang, and Robert W Heath. 2022. Integration of radar sensing into communications with asynchronous transceivers. *IEEE Communications Magazine* 60, 11 (2022), 106–112.

[69] Ying Zhang, Tingjing Wang, Huapeng Zhao, Yanxin Zhang, and Hua Zhao. 2017. Multiple radar subbands fusion algorithm based on support vector regression in complex noise environment. *IEEE Transactions on Antennas and Propagation* 66, 1 (2017), 381–392.

[70] Hongzi Zhu, Yiwei Zhuo, Qinghao Liu, and Shan Chang. 2018. π-splicer: Perceiving accurate CSI phases with commodity WiFi devices. *IEEE Transactions on Mobile Computing* 17, 9 (2018), 2155–2165.